Materials Research Bulletin 45 (2010) 1240–1249

Contents lists available at ScienceDirect

Materials Research Bulletin

journal homepage: www.elsevier.com/locate/matresbu

$Ca_3Co_4O_9$ ceramics consolidated by SPS process: Optimisation of mechanical and thermoelectric properties

Driss Kenfaui [a,*], Guillaume Bonnefont [b], Daniel Chateigner [a], Gilbert Fantozzi [b], Moussa Gomina [a], Jacques Guillaume Noudem [a]

[a] Laboratoire CRISMAT, UMR 6508 CNRS/ENSICAEN, Université de Caen Basse-Normandie, 6 Bd Maréchal Juin, 14050 Caen Cedex 04, France
[b] Laboratoire MATEIS - INSA, Bât. B. Pascal, 5° étage - 7, Avenue Jean Capelle 69621, Villeurbanne Cedex, France

ARTICLE INFO

Article history:
Received 14 October 2009
Received in revised form 26 April 2010
Accepted 7 May 2010
Available online 13 May 2010

Keywords:
A. Oxides
A. Ceramics
D. Thermal expansion
D. Mechanical properties

ABSTRACT

$Ca_3Co_4O_9$ (349) thermoelectric (TE) oxide ceramics were successfully prepared by Spark Plasma Sintering process. The effects of the uniaxial pressure (30–100 MPa), the dwell temperature (700–900 °C) and the cooling rate were investigated. Microstructure analyses have revealed strong enhancements of the bulk density as the pressure level and the applied temperature during the SPS process are increased. Mechanical properties were investigated by using instrumented nanoindentation and three point bending tests. Hardness, elastic modulus, strength and fracture toughness were shown to improve drastically and depend on the processing parameters. Thermal expansion measurements reveal a noticeable anisotropy induced by unidirectional hot pressing. The mechanical, thermal and thermoelectric properties were correlated to the microstructure and crystallographic texture of the resulting ceramics.

1. Introduction

Recent reports on thermoelectric (TE) materials have pointed out promising results on TE devices for the conversion of thermal energy from a temperature gradient into electrical energy (Seebeck effect) and *vice versa* (Peltier effect) [1]. Their TE efficiency is expressed by the figure-of-merit $ZT = (S^2 \times T)/(\rho \times \kappa)$, where Seebeck coefficient (S), electrical resistivity (ρ) and thermal conductivity (κ) are temperature (T) dependent materials properties. Hence a good TE material requires a high S, low ρ and low κ. The wide attention attached to the exploration of the TE materials, especially oxides, was launched just after Terasaki et al. [2] have found a large thermopower (100 $\mu V K^{-1}$ at 300 K) coexisting with a low resistivity (200 $\mu\Omega$ cm at 300 K) in $NaCo_2O_4$ single crystals. Three years after, layered cobalt oxides $Ca_3Co_4O_9$ (349) were reported [3,4] to possess fairly good TE performances, and unlike $NaCo_2O_4$ and other performing oxides like Bi–Ca/Sr–Co–O and Bi–Pb–Sr–Co–O [5–9], they resist oxidation in air at high temperature, are thermally and chemically stable and do not exhibit any polluting or toxic character. The 349 oxide phase is a misfit-layer structure with hexagonal CoO_2 layers, related to the CdI_2 type, and square Ca_2CoO_3 layers related to the NaCl type [4,10–12]. The edge-shared CoO_6 layers serve as electrons sink, and Ca_2CoO_3 layers can act as phonon scattering regions and reduce the thermal conductivity [12]. A ZT value of 0.87 at 973 K in air [13] was obtained for 349 single crystals, which however are still too small to be integrated in TE devices. Consequently, efforts have focused on 349 polycrystalline materials, needing the exploration of various processing methods with the aim to improve their properties *via* fully mastered microstructures. Hot-Pressing (HP), Magnetic Alignment (MA) and Spark Plasma Sintering (SPS) processes [8,14,15] have been shown to be efficient in the elaboration of dense and textured 349 ceramics, two main properties for a noticeable increase of their TE performances.

The most used process to date is Hot-Pressing, but the elaboration procedure is long and the resulting dense and high textured samples are too thin, unusable later for the different manipulations. In the present work, we report on $Ca_3Co_4O_9$ TE bulk ceramics consolidated by Spark Plasma Sintering. The influence of two monitored SPS parameters (i.e. the applied pressure level up to 100 MPa and the temperature from 700 to 900 °C) on materials characteristics is studied. The microstructure and texture features of the samples are investigated and correlated to the elaboration parameters, and are shown to govern the mechanical, thermal and TE properties.

2. Experiment

2.1. Processing conditions

The $Ca_3Co_4O_9$ (349) polycrystalline samples were prepared by conventional solid-state synthesis method. $CaCO_3$ and Co_3O_4 starting precursors in the stoichiometric ratio were meticulously

---

[*] Corresponding author. Tel.: +33 231 45 13 15; fax: +33 231 45 13 09.
E-mail address: driss.kenfaui@ensicaen.fr (D. Kenfaui).

0025-5408/$ – see front matter © 2010 Elsevier Ltd. All rights reserved.
doi:10.1016/j.materresbull.2010.05.006

mixed in dry conditions and calcined in air at 900 °C for 24 h to permit the carbonates decomposition, and then form the 349 phase. The obtained mixture was reground and treated in vacuum (10^{-3} bar) in the Spark Plasma Sintering (SPS) apparatus (Model: HP D 25/1, Fine Ceramics Technologies (FCT), Germany). For each sample, 3 g of 349 powders were loaded in a graphite die with an inner diameter of 20 mm. A pulsed electric current (2500 A, 4 V) was passed through the assembly to heat it up to the dwell temperature which was maintained for 2 min under a uniaxial pressure P.

A first series of four samples was prepared at 900 °C with a heating rate of 50 °C/min and under various stress levels: P = 30, 50, 75 and 100 MPa, in order to study the uniaxial pressure influence on the microstructure and correlate it to different properties of the 349 ceramics. The reference sample for this series was obtained by uniaxial cold pressing the 349 powder at 92 MPa into a 4.2 mm thick pellet with a diameter of 25 mm, followed by the conventional sintering at 920 °C for 24 h without any applied stress (0 MPa).

To examine the dwell temperature influence, a second series of five samples was processed by SPS under a stress level of 50 MPa but at different temperatures: 700, 750, 800, 850 and 900 °C, with a heating rate of 50 °C/min. Usually, the 349 ceramics are processed at 920 °C for 24 h by conventional sintering or hot pressing processes [16]. It is worth to remind that the heating mode used in SPS technique is unconventional; this is one of the motivations why we started to heat the material at 700 °C.

The cooling rate effect was also studied through the investigation of a third series of samples elaborated under 50 MPa and at 900 °C with a heating rate of 50 °C/min and at different cooling rates: 25, 50, 100 °C/min. A fourth sample was prepared using the same conditions (900 °C/50 MPa/2 min), but the heating was stopped at the end of the thermal dwell allowing the sample to be naturally cooled depending on the thermal inertia of the SPS system.

All the as-prepared samples (thickness $\sim$ 2 mm) were moderately heated at 600 °C for 2 h and then polished to remove the graphite foil used during SPS processing before further characterizations.

2.2. Microstructure investigations

The bulk density of 349 ceramics was measured by the Archimedes method (KERN & Sohn GmbH, Baligen, Germany). The microstructure was investigated using a Carl Zeiss (Supra 55, Oberkochen, Germany) Scanning Electron Microscope (SEM). Phase identification and texture studies were investigated by using X-ray diffraction on a 4-circle diffractometer setup equipped with a Curved Position Sensitive detector (CPS120 from INEL, Artenay, France), and by using the monochromatised Kα Cu radiation, as described in details elsewhere [17], and within the combined analysis formalism [18] implemented in MAUD [19]. Briefly, this methodology allows the quantitative texture determination of the samples, using a cyclic Rietveld refinement of a series of X-ray diagrams measured at different sample orientations. Due to the expected texture strength in such materials and the axially symmetric texture (induced by the deformation under uniaxial pressure), we measured 13 diagrams every 5° in tilt angle χ, for an incident angle of the X-ray beam on the sample of $\omega = 20^\circ$. The instrument contributions (χ and ω broadenings, peak shapes, zero-shifts) were calibrated using the 660b LaB_6 powder standard from NIST. A counting time of 10 min for each sample orientation was used, and our optical setup provides with a 0.1° peak widths in 2θ around $2\theta = 40^\circ$. Pole figures obtained here are normalised into multiples of a random distribution (mrd), a unit that does not depend on other factors than orientation. In such units, a sample without preferred orientations exhibits uniform pole figures with 1 mrd levels, while a textured sample shows pole figures with maxima and minima of orientation densities ranging from 0 mrd (absence of crystals oriented in this direction) to infinity (for a single crystal on few directions). The overall texture strength is evaluated through the texture index [20], which is expressed in mrd^2 units and varies from 1 (powder with random grains orientations) to infinity (perfect texture or single crystal) and used to compare the texture strength of different samples exhibiting similar orientation distributions (OD). Such normalised pole figures are calculated from the OD of crystallites, refined using the E-WIMV formalism [21] after extraction of the peak intensities during the Rietveld cycles. The OD and profile refinement reliabilities are estimated using conventional reliability factors [22]. During these refinements we used the supercell definition of 349 as previously [23]. We chose a sample reference frame in order that the pressure axis corresponds to the centre of our pole figure.

2.3. Mechanical tests

Instrumented nanoindentation tests were performed on the samples by using a XP Nano Indenter® (MTS Systems Corporation, Eden Prairie, MN) equipped with a Berkovich tip with a radius ≤20 nm. For each test, impressions were introduced on the mirror-polished sample sections which are perpendicular to the pressing axis, with 100 μm spacing between them in order to minimize the possible interaction between the deformed areas. After the indentation load was removed, the load-displacement (-penetration depth) data were used to calculate the hardness, H, and the elastic modulus (Young's modulus), E. The hardness for an indentation depth, h, can be calculated from the equation: $H = P/A$, where P is the load measured at the penetration depth, h, while A refers to the projected contact area between the indenter and the specimen for the load value P.

The elastic isotropic modulus of the specimen, E, is determined from the reduced modulus, E_r, given by: $E_r = (\sqrt{\pi} \times S_h)/(2 \times \beta \times \sqrt{A})$ where $S_h = \mathrm{d}P/\mathrm{d}h$ refers to the elastic stiffness of the specimen-indenter contact [24]. β is a constant that depends only on the used indenter (more or less symmetrical), and $\beta = 1.0615$ for a Berkovich tip [25].

In our experiments, we made use of the continuous stiffness measurements (CSM) option of the Nano Indenter® XP, which allowed the evaluation of the elastic contact stiffness S all along the loading path of the load-penetration curve.

The modulus, E, of the sample can then be calculated as follows: $E = (1 - \nu^2)/((1/E_r) - ((1 - \nu_i^2)/E_i))$ where ν and ν_i are the Poisson's ratios of the specimen and indenter respectively, and E_i is the elastic modulus of the indenter.

Three point bending tests were carried out at room temperature on 349 ceramics for measurement of the strength (fracture stress), σ_R. The tested bars were cut from the different samples with almost the same dimensions: thickness ~2 mm and width ~3 mm. The span was set at 12 mm. The load was applied in the direction parallel to the pressure axis during the SPS sintering.

Fracture toughness measurements were performed on SENB specimens with relative notch length $a_o/w \sim 0.33$ introduced by using a 50 μm thick saw.

2.4. Thermal measurements

The thermal expansion of the samples was assessed in the temperature range 50–900 °C. The measurements were performed in two directions: parallel and perpendicular to the applied pressure axis (out-plane and in-plane, respectively) for the samples of the first and second series.

2.5. Electrical measurements

The temperature dependence of the electrical resistivity, ρ, and Seebeck coefficient, S, were simultaneously measured in a

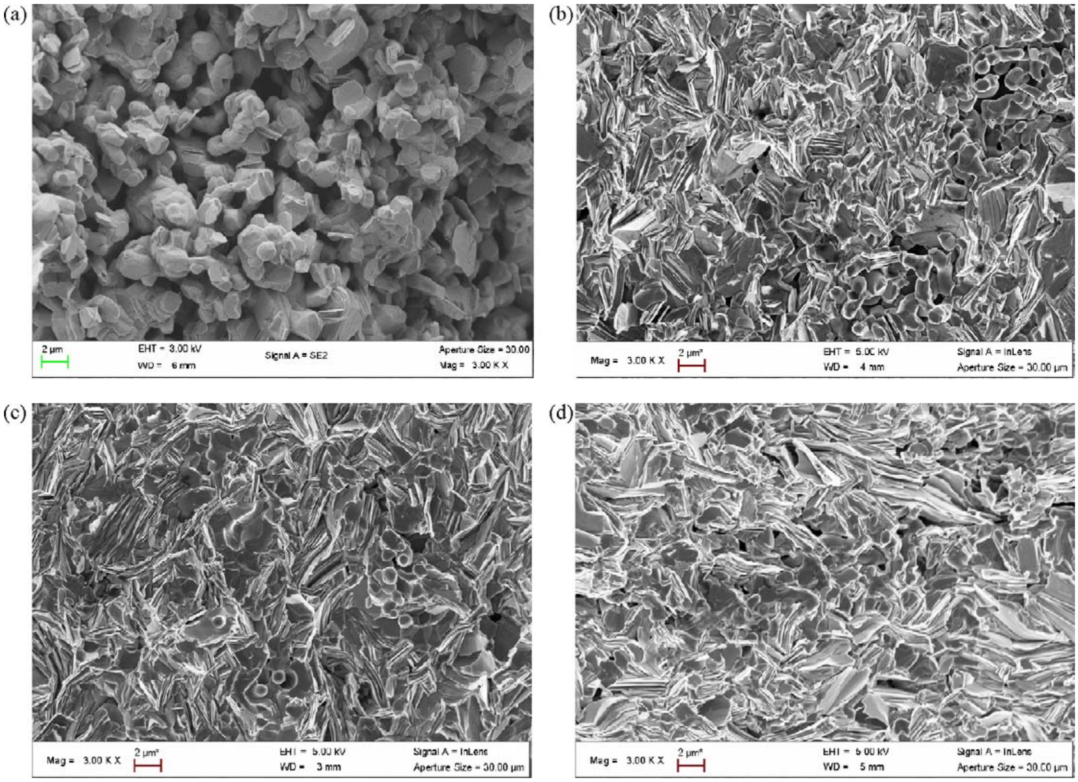

Fig. 1. SEM micrographs of fractured surfaces of the $Ca_3Co_4O_9$ ceramics: (a) reference sample processed without any applied stress and samples prepared by SPS process at 900 °C for 2 min and under (b) 30 MPa, (c) 50 MPa and (d) 75 MPa.

direction perpendicular to the pressure axis using a ZEM-3 apparatus (ULVAC-RIKO, Inc., Japan) in the temperature range from 350 to 900 K. These measurements were performed on ~2 mm × 2 mm × 10 mm bar-shaped specimens cut from the samples using a diamond saw.

3. Results and discussion

3.1. Microstructure

3.1.1. Pressure effect

Fig. 1 shows SEM micrographs of fractured surfaces of the reference sample (0 MPa) and samples of the first series consolidated under pressure levels of 30, 50 and 75 MPa. In the reference sample (Fig. 1a), grains with typical sizes less than 5 μm are loosely assembled and randomly oriented. A large porosity is also noted which points out the lack of homogeneity responsible for the noticeable low bulk density (60% of the theoretical density). That may impair the mechanical and electrical properties. Under the chosen SPS conditions, at 30 MPa (Fig. 1b), the grains exhibit roughly platelet-like shape with a tendency to align and stack their planes perpendicularly to the applied pressure axis (vertical axis of the micrographs). The mean grain size is increased to 8 μm compared to the reference sample. A large number of pores are eliminated, which results in strengthening noticeably the bulk density to 98.3%. Nevertheless, limited porous zones still remain, together with smaller and more isotropic grains comparable to the ones of Fig. 1a, indicating the incompleteness of the reaction process. At 50 MPa (Fig. 1c), the bulk density is raised to 99.6% and almost all the porous zones disappear. However, we observe neither a significant enhancement of the platelet alignment nor an increase of the platelet size as compared to the sample prepared at 30 MPa. This limitation is probably due to the additional horizontal pressure applied [26] on the sample by the die walls which competes with the uniaxial applied pressure. As the sample is constrained within the die walls, its deformation is hindered and the grain rotation blocked when the porosity is removed. The sample consolidated at 75 MPa (Fig. 1d) shows a densified structure containing weak zones exhibiting a number of pores and smaller grains, although the porous zone sizes were already greatly reduced upon processing at 50 MPa. It may be due to the further applied stress during the short dwell time of 2 min. The resulting sample bulk density slightly decreases to 98.5%. The newly developed porous zones are limited for a much larger pressure of 100 MPa thereby allowing an enhancement of the bulk density (99.2%).

3.1.2. Dwell temperature effect

Fig. 2 illustrates the SEM micrographs of surfaces of rupture of the samples from the second series prepared at 700 and 850 °C. The mean grain size decreased, with values smaller than 2.5 μm (Fig. 2a), in comparison to the reference sample sintered without any applied stress (0 MPa). Despite a pressure level of 50 MPa, the microstructure shows some pores and the grains are randomly oriented for the 700 °C processing temperature. The bulk density is 95.7% of the theoretical density. Almost similar microstructures are observed for the samples prepared at 750 and 800 °C, with however a larger bulk density: 96.2 and 97.2% respectively. A denser structure is obtained (Fig. 2b) as the dwell temperature is increased (98.3% for 850 °C): grains with sizes up to 6.5 μm are observed along the platelet planes. The largest pores are eliminated but no enhancement in grains alignment was noted. The bulk density was larger for the sample consolidated at 900 °C, which exhibits larger platelet shaped grains somewhat oriented (Fig. 1c).

The cooling rate does not induce any noticeable influence on the sample microstructure (third series) whatever the chosen cooling rate in the 25–100 °C/min range. The same microstructure was also observed for the fourth sample cooled naturally after the dwell

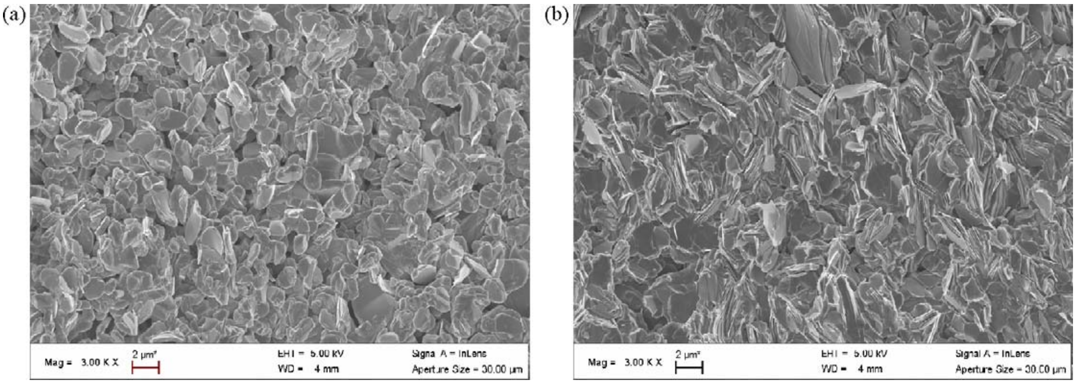

Fig. 2. SEM micrographs of fractured surfaces of the $Ca_3Co_4O_9$ samples prepared by SPS process under 50 MPa for 2 min and at (a) 700 °C and (b) 850 °C.

time. The microstructures of the samples from this series are similar to the one observed in Fig. 1c.

3.2. Crystallographic texture

When inclining the sample from $\chi = 0$ to 60° (Fig. 3), one can typically see a strong decrease of the 00ℓ lines (at 2θ around 33° for instance), as an indication of a preferred orientation component with the *c*-axis aligned with the pressure axis ($\chi = 0$ value). However, such diagrams show direct diffracted intensities and are then dependent, for instance, on sample porosities.

They consequently cannot be directly compared from one sample to each other, on an orientation point of view. The diagram fits using the combined analysis (Fig. 3) provide the necessary parameters for orientation comparisons. The fits were achieved within satisfactory reproduction of the experimental spectra, as can be visually seen on two-dimensional plots of measured and refined diagrams (Fig. 4), and from the low Rietveld Goodness-of-Fit and OD weighted reliability factors (Tables 1 and 2), not larger than 4.3 and 6.8% respectively.

One can observe a slight overall variation of the cell-parameters *a*, *b* and *c*, which decreases with the applied pressure (Table 1), but not with the dwell temperature (Table 2). The orientation of crystallites is indeed achieved within a cyclic-fibre texture component (i.e. the mean *c*-axis are aligned along the fibre axis [18]), with the fibre axis parallel to the pressure axis (Fig. 5). The cyclic-fibre is however not the only orientation component present, even if the ODF minima are 0 mrd for all the samples, as will be discussed later, as can be seen from the slight reinforcement of the periphery of the {0 0 1} pole figure.

The distribution of the cyclic-fibre orientation component is large compared to previously published textures observed on the same materials prepared using other elaboration methods. The maximum value of the {0 0 1} pole figures (Tables 1 and 2) is consequently relatively low, not larger than 4.05 mrd. The obtained values of the {0 0 1} maximum indicate a small increase of the main texture component strength with applied pressure, but its significant decrease at 100 MPa. Compared to the reference sample, the texture strengths obtained using SPS are about 0.2–0.6 mrd more pronounced, looking at the {0 0 1} pole figure maximum. One could interpret this as a small interest for using the SPS technique. However, the reference sample has been obtained by cold pressing at 92 MPa, while the texture strengths increase using SPS are observed as soon as 30 MPa is applied, thanks to the crystal growth as platelets. Furthermore, since the texture strength is shown to start decreasing for 100 MPa, cold pressing at 92 MPa is probably close to the limit in uniaxial pressure one could apply in the aim of increasing the texture levels.

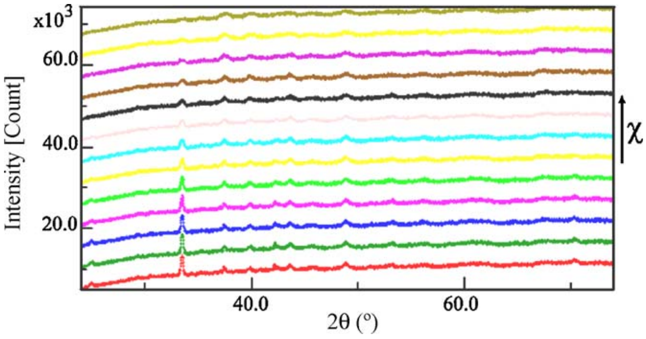

Fig. 3. 2θ diagrams measured for every χ-orientation of the sample elaborated at 30 MPa and 900 °C, from $\chi = 0^\circ$ (bottom) to $\chi = 60^\circ$ (top).

For relatively small texture strengths as is the case here [22], the texture strength increase becomes more noticeable when looking at texture index or maxima of the OD (Tables 1 and 2).

Comparatively, for a 50 MPa applied pressure, the {0 0 1} maximum increase of the cyclic-fibre component is more pronounced with the dwell temperature up to 900 °C. Higher temperatures then ease the achievement of larger texture strengths during the SPS process.

A secondary orientation component observed as the {0 0 1} pole figure periphery reinforcement, develops both for the lower applied pressures and temperatures (Fig. 6), then tends to disappear under optimised conditions, however without complete extinction. This texture component corresponds to *c*-axis aligned

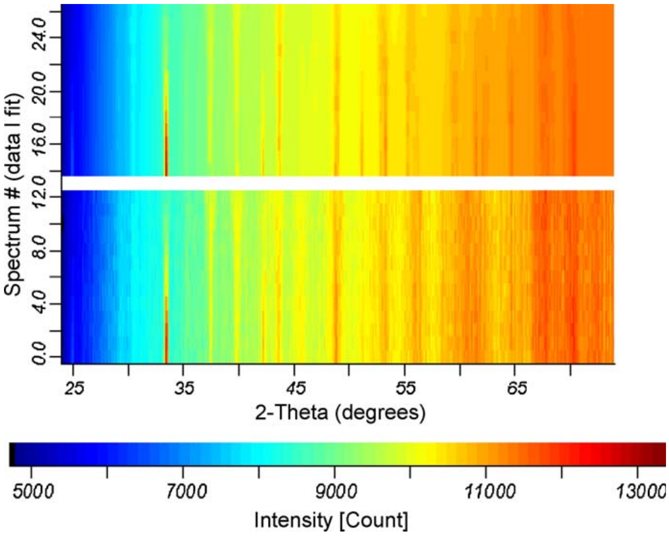

Fig. 4. Two-dimensional measured (bottom) and refined (top) 2θ diagrams measured for every χ-orientation of the sample processed under 30 MPa at 900 °C.

Table 1
Refined parameters obtained from X-ray combined analysis of the samples prepared at 900 °C under various pressure levels. Digits in parenthesis are estimated standard deviations from the refinements.

Stress (MPa)	0	30	50	75	100
Cell parameters					
a (Å)	4.8427(6)	4.834(2)	4.8160(6)	4.821(1)	4.8098(5)
b (Å)	36.561(3)	35.99(2)	36.267(6)	36.233(9)	36.149(5)
c (Å)	10.8390(7)	10.841(4)	10.7996(3)	10.8016(7)	10.7849(7)
β (°)	97.96(1)	98.02(3)	98.049(6)	98.03(1)	97.984(8)
Rietveld GoF	1.33	4.27	3.85	1.32	2.99
OD R_w (%)	6.81	6.21	1.86	3.33	1.88
F^2 (mrd^2)	5.80	3.15	6.36	6.92	6.03
OD maximum (mrd)	27.68	20.85	29.10	31.92	29.78
{0 0 1} pole fig. max (mrd)	3.5	3.74	3.94	4.05	3.49

Table 2
Refined parameters obtained from X-ray combined analysis of the samples processed under 50 MPa at various dwell temperatures. Digits in parenthesis are estimated standard deviations from the refinements.

Temperature (°C)	700	750	800	850	900
Cell parametres					
a (Å)	4.8164(3)	4.8179(3)	4.8083(5)	4.8115(6)	4.8160(6)
b (Å)	36.516(3)	36.563(3)	36.393(5)	36.144(5)	36.267(6)
c (Å)	10.8018(5)	10.8144(5)	10.7885(6)	10.7823(4)	10.7996(3)
β (°)	98.403(7)	98.371(5)	98.44(1)	98.011(8)	98.049(6)
Rietveld GoF	3.86	4.09	1.50	2.97	2.99
OD R_w (%)	2.00	3.55	2.99	1.76	1.88
F^2 (mrd^2)	4.95	6.07	6.35	6.55	6.36
OD maximum (mrd)	21.89	24.15	33.89	36.77	29.10
{0 0 1} pole fig. max (mrd)	2.29	2.15	3.14	3.41	3.94

perpendicularly to the pressure axis, with other crystal directions randomly oriented around the *c*-axis, i.e. in a cyclic-planar texture pattern [18]. Such a component is undesired from the physical properties point of view, since it corresponds to, on one hand, crystals exhibiting a larger resistivity along the sample plane targeted for use (perpendicular to the pressure axis), and on the other hand, to the creation of large angle grain boundaries. However, this component appears difficult to avoid using SPS. Even at a pressure of 100 MPa (Fig. 6a), it does not completely disappear, though a pronounced decrease is observed for applied stresses larger than 30 MPa. The dwell temperature also does not help in removing furthermore this component, even if a temperature larger than 800 °C seems necessary for its strong decrease. One should notice that this temperature corresponds to the achievement of a microstructure with platelet-like crystals (Figs. 1c and 2b). Indeed, for a too much low temperature (≤800 °C), the crystals still exhibit a more rounded shape, which does not allow an easy crystal orientation even under 50 MPa (Fig. 6b, top three {0 0 1} pole figures), producing at least two low-strength orientation components. But, for a high enough temperature like 900 °C, at small pressures like 30 MPa (Fig. 6a), the residual pressure applied by the die wall partly overcomes the applied stress and creates the secondary texture components. It then finally appears that using SPS, high enough temperatures and applied pressures are required to allow the development of anisotropic crystallite shapes and orient these latter under a uniaxial pressure field, respectively. Under our conditions the transverse applied pressure field from the die walls always gives rise to a secondary texture components that can be decreased by a reasonable amount for pressures around 50 MPa. At applied pressures higher than 75 MPa (Fig. 6a), the main texture component strength starts decreasing again, giving rise to its significant distribution broadening.

3.3. *Mechanical properties*

3.3.1. *Pressure effect*

For each investigated sample, a batch of nine impressions, arranged in a 3 × 3 pattern, was made. The pattern of residual impressions, left on an area of the sample prepared at 50 MPa in the first series after the Berkovich tip was withdrawn, is shown on the microphotograph of Fig. 7.

The average values of the hardness, *H*, the Young's modulus, *E*, and the strength, σ_R, obtained for the samples of the first series are plotted versus the applied pressure in Fig. 8a. Mechanical properties of our samples improve drastically with the applied pressure, with *H* and *E* spanning from 0.11 ± 0.03 to 2.34 ± 0.14 GPa and from 10 ± 2 to 74 ± 3 GPa as the pressure level raises from 0 to 30 MPa, respectively. σ_R exhibits a similar evolution, increasing from 18.4 ± 2.5 MPa for the reference sample to 252 ± 9 MPa for the sample consolidated at 30 MPa. In this pressure range, the bulk density of the 349 ceramics is greatly strengthened from 60 to 98.3% while the maximum density of the {0 0 1} pole figures only increases from 3.5 to

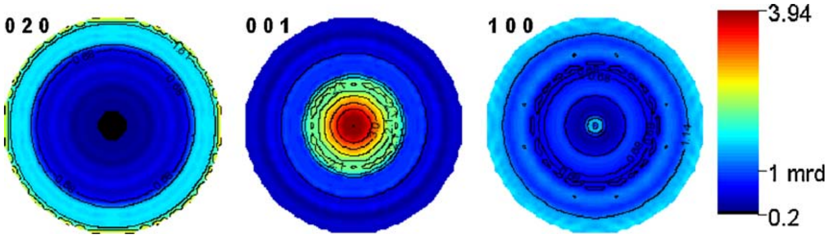

Fig. 5. {0 2 0}, {0 0 1} and {1 0 0} recalculated normalised pole figures for the sample processed under 30 MPa at 900 °C.

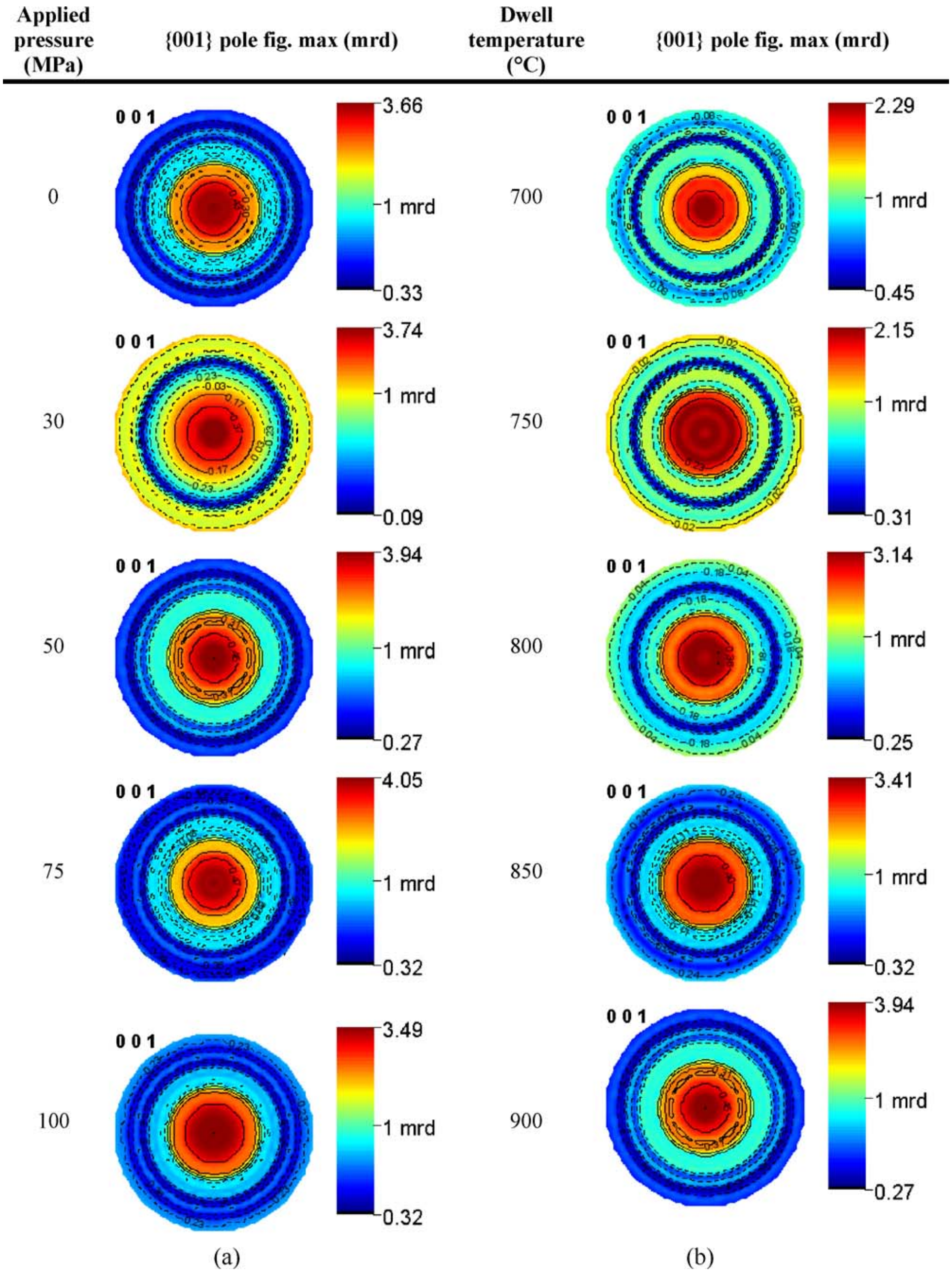

Fig. 6. {1 0 0} pole figures maximum obtained for (a) the samples processed under various pressure levels (first series) and (b) for those sintered at various dwell temperature (second series). A secondary orientation component observed as the {0 0 1} pole figure periphery reinforcement, develops both for the lower applied pressures and temperatures.

3.74 mrd. The mechanical behaviour improvement is then essentially related to the strong densification of the ceramics in this pressure range. Above 30 MPa, *H*, *E* and σ_R show a slower increase with the pressure level. That indicates the majority of the pores are eliminated at low pressure levels and an important part of the bulk density improvement is obtained for pressure levels not higher than 30 MPa, densification becoming more and more difficult for higher pressure values. This can explain such slow evolution of the mechanical properties at high stress levels, with a stabilisation of *H* and *E*, especially without any significant evolution of the texture. The hardness reaches its maximum value of 3.2 ± 0.4 GPa for very dense samples obtained at 100 MPa. The Young's Modulus, *E*, remains in the 82 ± 6–87 ± 5 GPa range for pressures larger or equal to 50 MPa. The strength reaches 282 ± 8 MPa at 50 MPa, corresponding to 15 times the reference sample value. We notice a decrease of about 30 MPa in σ_R when the pressure is varied from 50 to 75 MPa, while this reduction is not observed at 100 MPa. The smallest σ_R value observed for 75 MPa is attributed to microstructure changes, i.e. the presence of weak and porous zones. Although their presence is not associated to low *E* value, these defects may bring discredit on these materials for use in devices.

Concerning the fracture toughness, K_{IC} (Fig. 9a), it appears that SPS densification is an effective way for increasing the reliability of 349 ceramics as the porosity and size of defects are reduced. K_{IC} increases rapidly as the uniaxial pressure is applied during the sintering. An improvement of more than 7 times is obtained in K_{IC} under 30 MPa. K_{IC} topped at 2.92 ± 0.05 MPa m$^{1/2}$ for 50 MPa, which imparts the highest bulk density. Like σ_R, K_{IC} is slightly decreased for pressure higher than 50 MPa, which is coherent with the microstructure features. SEM observations show that failure proceeds by intergranular fractures.

Consequently, better mechanical properties, displaying a considerable improvement compared to the conventionally

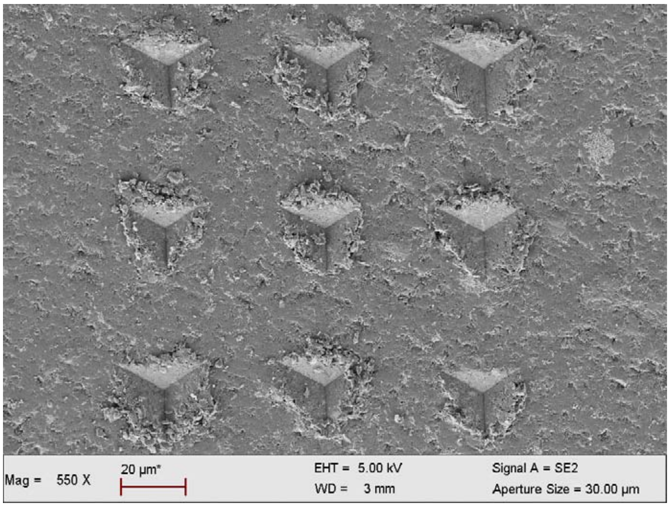

Fig. 7. A 3 × 3 matrix pattern of residual impressions introduced on a surface perpendicular to the SPS pressing axis of the sample prepared by SPS process under 50 MPa.

sintered sample (reference sample), are found for 349 ceramics consolidated by the SPS process operated at pressures equal or higher than 50 MPa. Taking into account microstructure analysis and tiny mechanical properties improvements at higher pressure levels, the optimal pressure level for samples of the first series is 50 MPa.

3.3.2. Dwell temperature effect

Fig. 8b shows that the hardness, elastic modulus, and strength, increase monotonously as the dwell temperature is raised. That may be explained by the increase in the bulk density with temperature and by a slight difference in the chemical compositions. Indeed, *H* and *E* only increase with about 0.1 and 3 GPa, respectively, when the dwell temperature raises from 700 to 750 °C. The samples processed at these temperatures have the same chemical composition. They have still a small amount of carbonates in the 349 phase, therefore the small enhancement in mechanical properties correlates essentially to the slight increase in bulk density (∼5%). σ_R exhibits an enhancement of about 29 MPa in this temperature range. When the dwell temperature is raised from 750 to 800 °C, the composition is not modified, but the bulk density is significantly reinforced (97.2%), which induces consequent enhancements in *H*, *E* and σ_R, corresponding to 0.73, 20.4 GPa, and 81.7 MPa, respectively. Similar improvements of *E* and σ_R are noticed, but a larger increase of *H*, when the dwell temperature is raised from 800 to 850 °C. That may be due to the chemical composition change and densification strengthening. Since the samples processed by SPS at 850 and 900 °C exhibited the same composition, stronger densification obtained at 900 °C results in higher mechanical properties. At this later temperature, $H = 2.62 \pm 0.2$ GPa, $E = 73.42 \pm 2.53$ GPa and $\sigma_R = 285 \pm 6$ MPa, i.e. an improvement of 7.9, 3.6 and 9.3 times, respectively, compared to the sample processed at 700 °C.

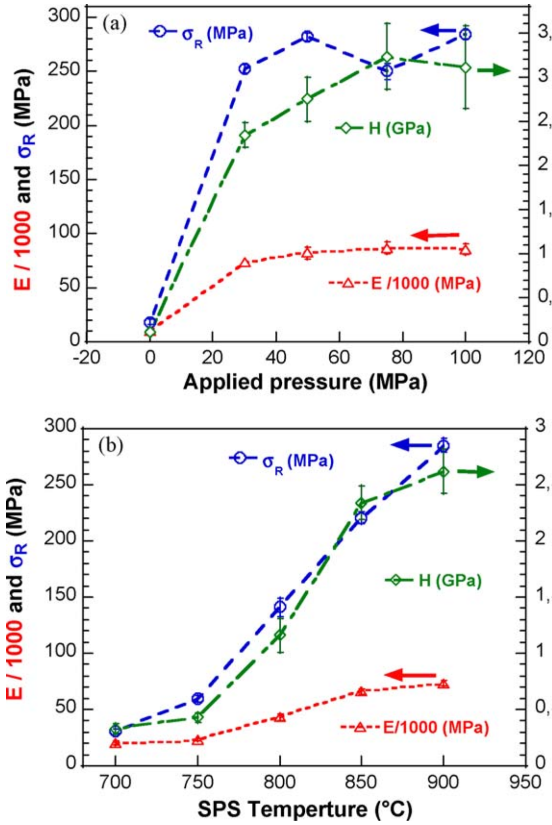

Fig. 8. (a) Hardness, *H*, elastic modulus, *E*, and strength, σ_R, versus the pressure level for the samples of the first series processed at 900 °C for 2 min. (b) *E*, *H* and σ_R versus the dwell temperature for the samples of the second series processed at 50 MPa for 2 min.

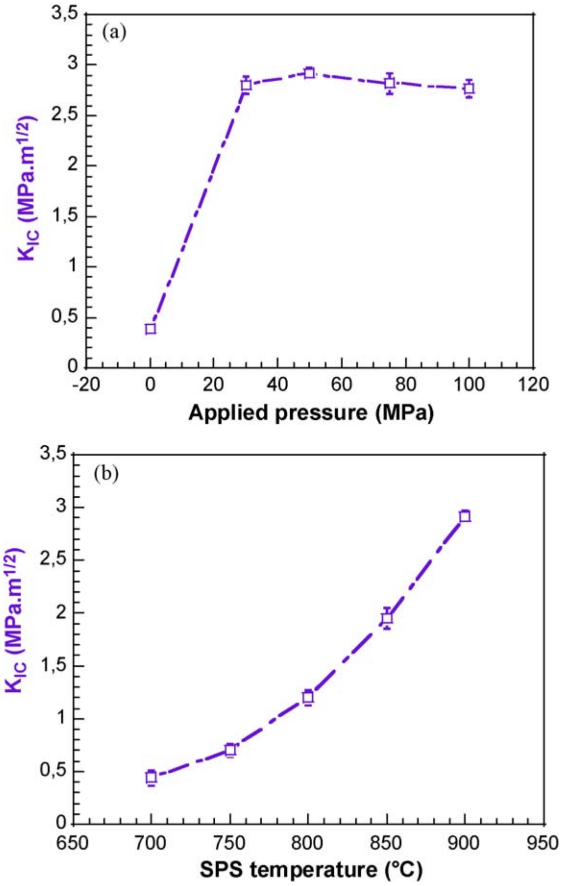

Fig. 9. Average fracture toughness K_{IC} obtained for (a) the samples of the first series processed under various pressure levels at 900 °C for 2 min and (b) the samples of the second series processed at various dwell temperatures under 50 MPa for 2 min.

The fracture toughness K_{IC} exhibited a similar evolution (Fig. 9b). K_{IC} monotonously increases with the dwell temperature, and reaches its highest value at 900 °C.

Finally, for the second series of samples, the best mechanical properties are obtained for 349 ceramics processed at 900 °C. Also, the cooling rate has no influence on the mechanical properties for this dwell temperature.

Consequently, the higher mechanical properties are expected for a thermomechanical sintering cycle with 50 MPa pressing stress level and 900 °C dwell temperature.

3.4. Thermal analysis

The two-dimensional nature of the thermal behaviour for 349 ceramics processed by SPS is evidenced in Fig. 10a. It shows the thermal expansion measured in the temperature range 50–900 °C for the reference sample (0 MPa) and, in the directions parallel and perpendicular to the pressure axis (out-of-plane and in-plane, respectively), for the sample processed at 900 °C and under 50 MPa. It should be noticed a clear difference in the thermal behaviour along the heating and the cooling paths, which highlights the effects of irreversible phenomena produced at the grain boundaries during the thermal cycle. One observes a remarkable difference in thermal behaviour for two crystallographic directions. Indeed, the linear thermal expansion of the reference sample lies between the in-plane and out-plane ones of the specimen consolidated by SPS. The coefficient of thermal expansion (CTE) of the reference sample is $\alpha_{\mathrm{ref}} = 12.6 \times 10^{-6}\ \mathrm{K}^{-1}$ while those of the SPS sample determined in out-of-plane and in-plane are $\alpha_c = 15.75 \times 10^{-6}\ \mathrm{K}^{-1}$ and $\alpha_{ab} = 6.3 \times 10^{-6}\ \mathrm{K}^{-1}$, respectively. These results ($\alpha_c/\alpha_{ab} = 2.5$) point out the influence of densification (porosity reduction) and grain fineness (increased grains boundaries density) imparted by SPS processing.

The out-of-plane and in-plane CTEs (α_c and α_{ab}) versus the applied pressure for the samples of the first series are plotted in Fig. 10b. The α_{ab} values correlate well with the microstructure analysis. α_{ab} decreases as the applied pressure is raised up to 50 MPa, which is essentially related to the improvement of the connections between the grains. The slight increase observed in the in-plane grain size induces a diminution of the in-plane grains boundaries density, which may also be a reason for α_{ab} reduction. Above 50 MPa, α_{ab} is increased due obviously to the bulk density decrease observed for higher applied pressures. α_c seems to increase monotonously with the applied pressure, showing an approximate linear trend. The α_c rise is probably attributed to the increment of the out-of-plane grains boundaries density induced by the reduction of the out-of-plane grains size under the pressure effect.

The out-of-plane and in-plane CTEs versus the dwell temperature for the samples of the second series are also given in Fig. 10c. α_{ab} clearly exhibits a monotonous diminution with the dwell temperature as a consequence of the bulk density enhancement, whereas α_c shows a linear monotonous increase.

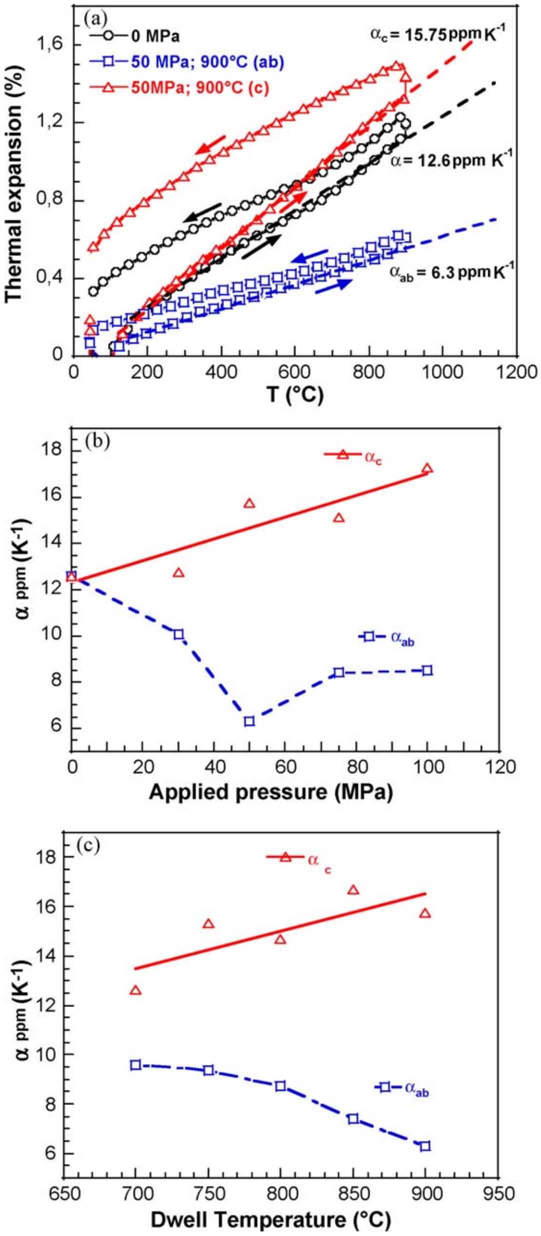

Fig. 10. (a) Thermal expansion measured in the temperature range 50–900 °C for the reference sample (0 MPa) and in out-of-plane and in-plane of the sample processed at 900 °C and under 50 MPa. The out-of-plane and in-plane CTEs (α_c and α_{ab}) versus (b) the pressure level and (c) the dwell temperature for the samples of the first and second series, respectively.

3.5. Transport properties

3.5.1. Pressure effect

Fig. 11a shows the temperature dependence of the electrical resistivity, $\rho(T)$, for the different pressure levels, in the 350–900 K temperature range. The current was injected perpendicular to the pressure axis, i.e. the current flows along the mean (a, b) planes of the samples. All curves show a ρ monotonous decrease with the temperature. ρ is strongly reduced as the processing pressure level is raised up to 30 MPa compared to the reference sample (Fig. 11a). This is again mainly due to the strong density enhancement from 60 to 98.3% in this pressure range, but also secondarily to a slightly larger texture strength achievement. Such material compaction and alignment facilitates the current circulation by removing a large number of pores and a number of grain boundaries, and improving the connection between grains. The lowest values of the resistivity are obtained for the sample processed at 50 MPa, which is denser and from which the weak porous zones are eliminated, compared to the sample prepared at 30 MPa. This later resistivity reduction correlates with a higher grain contact quality, the suppression of almost all weak zones, and the texture strength improvement at a processing pressure of 50 MPa. The resistivity, $\rho_{840\ \mathrm{K}}$, recorded at this pressure is 9.3 mΩ cm, which is almost 4.5 times smaller than that of the reference sample. This value is in agreement with that reported by Zhou et al. [8] on 349 oxides processed by SPS.

For the samples processed at higher pressure levels (75 and 100 MPa), $\rho(T)$ shows an upward trend because of the “reappearance” of the weak zones. The slightly lower resistivity of the sample processed at 100 MPa compared to the one elaborated at 75 MPa can be explained by the slight gain in bulk density, even though its texture shows a lower strength. One can see in this analysis, that the competition between porosity reduction, crystallite orientations and increase in grain boundaries density, attributes a much larger role to densification for obtaining lower resistivity.

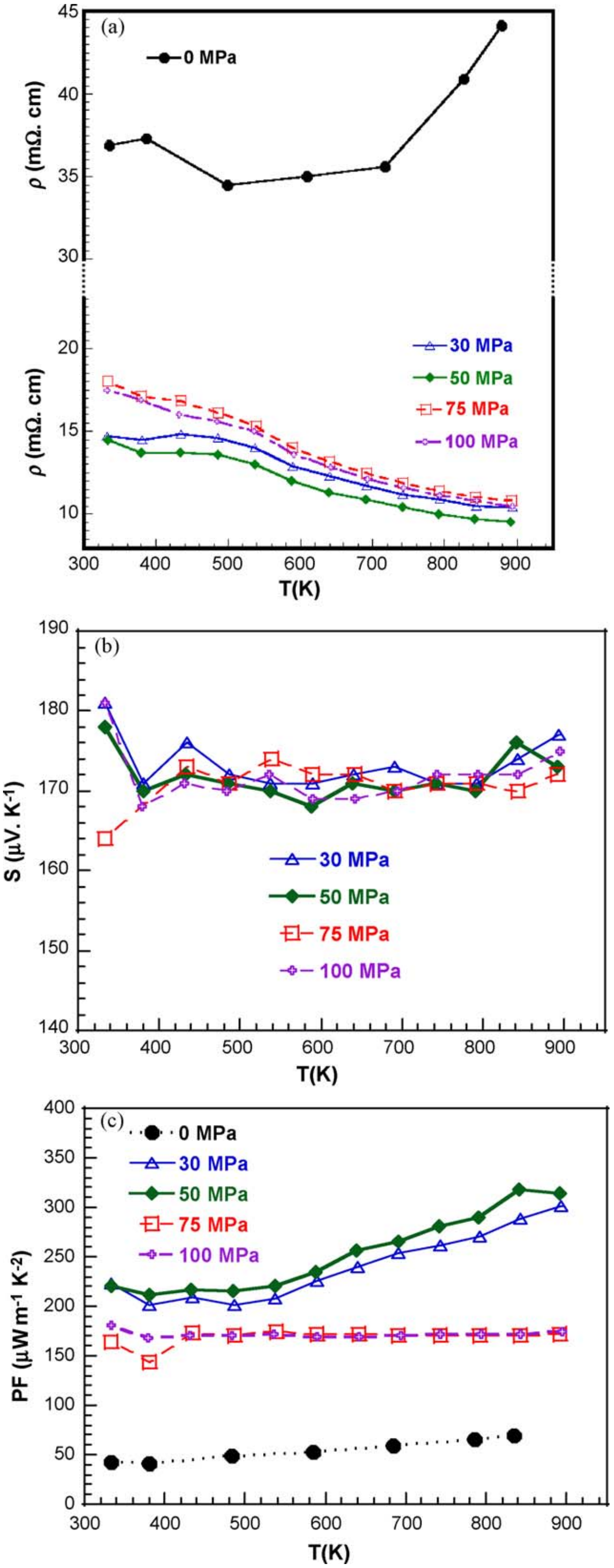

Fig. 11. Temperature dependence of (a) electrical resistivity, ρ, (b) Seebeck coefficient, S, and (c) power factor, $PF = s^2/\rho$, for 349 samples of the first series processed by SPS under various pressure levels.

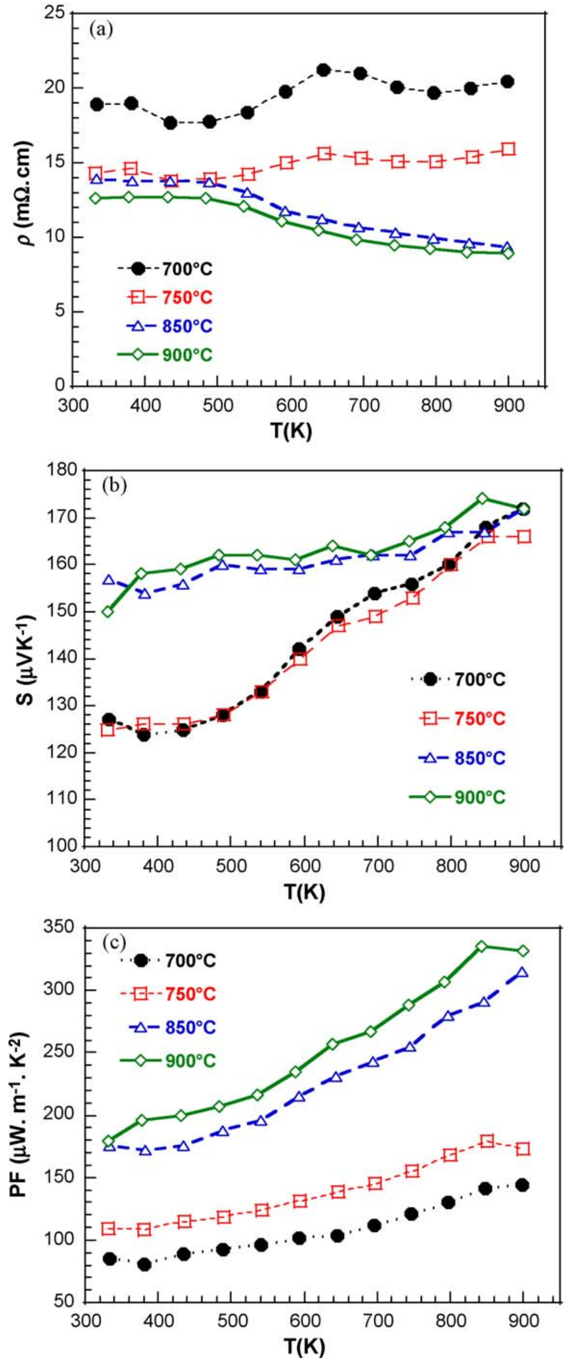

Fig. 12. Temperature dependence of (a) electrical resistivity, ρ, (b) Seebeck coefficient, S, and (c) power factor, $PF = s^2/\rho$, for 349 samples of the second series processed by SPS process at various temperatures.

Fig. 11b shows the temperature dependence of the Seebeck coefficient, $S(T)$, measured also in the direction perpendicular to the pressure axis. The S values are nearly independent of the applied pressure and a value of 176 μV K^{-1} at 840 K is recorded for the sample processed at 50 MPa. The positive value of S indicates that the majority of the charge carriers is hole-like and the values observed on our 349 ceramics are consistent with data published in the literature [8,15,27]. Since ρ is reduced without decreasing S, the power factor, $PF = S^2/\rho$, improves with the processing pressure and reaches 315 μW m^{-1} K^{-2} at 840 K for the sample processed at 50 MPa (Fig. 11c). This PF value is larger than that reported for 349 ceramics processed by SPS [8,27].

These results show that the 349 ceramics exhibiting optimal TE properties are those processed by SPS at 50 MPa, the optimal pressure level applied in the configuration used for samples preparation of the first series.

3.5.2. Dwell temperature effect

The temperature dependence of the electrical resistivity (Fig. 12a) shows a decreasing trend for the samples processed at higher dwell temperatures (850 and 900 °C), i.e. for the denser samples, after a small plateau in the 300–500 K range, and an increasing trend for the samples processed at lower dwell temperatures (700 and 750 °C). The plateau value of the resistivity is the same as for the sample processed at 750 °C. This shows that between 750 and 850 °C, the temperature effect on grain contacts is mainly a change of their conduction behaviour, from a metallic-like to a semiconducting-like character. Taken as all, the resistivity is remarkably reduced as the dwell temperature is raised. Such reduction in ρ mainly correlates to the bulk density strengthening and to a lesser extent to the grains size increase and the texture of the 349 ceramics for the lower dwell temperatures. For the largest dwell temperatures analyzed here, the ρ decrease is attributed to a change of the grain boundary conductive character.

The thermopower versus temperature, $S(T)$, for the different dwell temperatures is presented in Fig. 12b. The samples processed at 700 and 750 °C exhibit almost the same values, but lower than those of the samples prepared at 850 and 900 °C, up to approximately 850 K for which all the samples exhibit roughly the same S value. The difference in the behaviours of these two sets of samples originates from their compositions. As a consequence, the power factor, PF, improves with the dwell temperature (Fig. 12c), the largest PF value of about 315 μW m^{-1} K^{-2} being associated with the highest S and lower ρ values measured on samples obtained at 900 °C.

As it was already mentioned above about the mechanical properties, TE characterization of the third series of samples has not shown any influence of the cooling rate on the 349 ceramics TE performances.

4. Conclusions

$Ca_3Co_4O_9$ (349) dense ceramics have been elaborated using Spark Plasma Sintering. The effects of different processing parameters were investigated: pressure level, dwell temperature and cooling rate. The pressure level and the dwell temperature strongly influence the microstructure in terms of density, while the cooling rate does not. For dwell temperature of 900 °C, the optimum pressure level is 50 MPa. The observed texture levels are relatively low compared to that induced by hot pressing technique, and not above 4.05 mrd for the {0 0 1} pole figure maximum. The low texture strength is partly explained by a competition of two perpendicular pressure fields in our SPS configuration, giving rise to two orientation components. Such texture strengths are shown to have much less influence on TE and mechanical properties than bulk density. The mechanical properties were shown to improve drastically with the pressure level. Hardness, H, Young's Modulus, E, strength, σ_R, and fracture toughness, K_{IC}, are distinctly improved to 3.2 ± 0.4, 82 ± 6 GPa, 282 ± 8 MPa and 2.92 ± 0.05 MPa m$^{1/2}$, respectively, compared to the conventional sintered sample without any applied stress ($H = 0.11 \pm 0.03$ GPa, $E = 10 \pm 2$ GPa, $\sigma_R = 18.4 \pm 2.5$ MPa and $K_{IC} = 0.39 \pm 0.02$ MPa m$^{1/2}$). These properties were found also to increase monotonously with the dwell temperature. Thermoelectric properties noticeably increased with the dwell temperature and the pressure level up to 50 MPa. The power factor reaches 315 μW m^{-1} K^{-2} at 840 K for the sample processed at 50 MPa.

The determined optimum thermomechanical cycle is currently applied for elaborating 349 ceramics in a new SPS configuration allowing stronger texturation and densification of these materials.

Acknowledgments

D. Kenfaui and the co-authors acknowledge the "Conseil Régional de Basse-Normandie, France" for its Ph.D. fellowship funding and financial participation to the experimental setup used in this work. They also would like to acknowledge "*MATEIS-INSA* laboratory *at Lyon*, *France*" for SPS samples preparations. The authors thank Mr. J. Lecourt and Ms. Kennard for their help during the 349 powders synthesis.

References

[1] E.J. Winder, A.B. Ellis, G.C. Lisensky, J. Chem. Educ. 73 (1996) 940–946.

[2] I. Terasaki, Y. Sasago, K. Uchinokura, Phys. Rev. B 56 (1997) 12685–12687.

[3] S. Li, R. Funahashi, I. Matsubara, K. Ueno, H. Yamada, J. Mater. Chem. 9 (1999) 1659–1660.

[4] A.C. Masset, C. Michel, A. Maignan, M. Hervieu, O. Toulemonde, F. Studer, B. Raveau, Phys. Rev. B 62 (2000) 166–175.

[5] M. Hervieu, Ph. Boullay, C. Michel, A. Maignan, B. Raveau, J. Solid State Chem. 142 (1999) 305–318.

[6] G. Xu, R. Funahashi, M. Shikano, I. Matsubara, Y. Zhou, J. Appl. Phys. Lett. 80 (2002) 3760–3762.

[7] R. Funahashi, I. Matsubara, S. Sodeoka, Appl. Phys. Lett. 76 (2000) 2385–2387.

[8] Y. Zhou, I. Matsubara, S. Horii, T. Takeuchi, R. Funahashi, M. Shikano, J.I. Shimoyama, K. Kishio, W. Shin, N. Izu, N. Murayama, J. Appl. Phys. 93 (2003) 2653–2658.

[9] A. Maignan, S. Hébert, D. Pelloquin, C. Michel, J. Hejtmanek, J. Appl. Phys. 92 (2000) 1964–1967.

[10] K. Koumoto, I. Terasaki, R. Funahashi, Mater. Res. Bull. 31 (2006) 206–210.

[11] K. Takada, H. Sakurai, E. Takayama-Muromachi, F. Izumi, R.A. Dilanian, T. Sasaki, Nature (London) 422 (2003) 53–55.

[12] Y. Miyazaki, K. Kudo, M. Akoshima, Y. Ono, Y. Koike, T. Kajitani, Jpn. J. Appl. Phys. Lett. 39 (2000) 531–533.

[13] M. Shikano, R. Funahashi, Appl. Phys. Lett. 82 (2003) 1851–1853.

[14] M. Prevel, S. Lemonnier, Y. Klein, S. Hébert, D. Chateigner, B. Ouladdiaf, J.G. Noudem, J. Appl. Phys. 98 (2005) 93706–93709.

[15] Y. Zhang, J. Zhang, Q. Lu, Ceram. Int. 33 (2007) 1305–1308.

[16] D. Kenfaui, D. Chateigner, M. Gomina, J.G. Noudem, Anisotropy of the mechanical and thermoelectric properties of hot-pressed single-layer and multi-layer thick $Ca_3Co_4O_9$ ceramics. Int. J. Appl. Ceram. Technol., doi:10.1111/j.1744-7402.2009.02431.x.

[17] J. Ricote, D. Chateigner, Bol. Soc. Esp. Ceram. Vidrio 38 (1999) 587–591.

[18] D. Chateigner (Ed.), Combined Analysis: Structure-Texture-Microstructure-Phase-Stresses-Reflectivity Analysis by X-ray and Neutron Scattering, ISTE, London, 2004, pp. 147. Available at http://www.ecole.ensicaen.fr/~chateign/texture/combined.pdf.

[19] L. Lutterotti, S. Matthies, H.R. Wenk, MAUD (Material Analysis Using Diffraction): a user friendly Java program for Rietveld texture analysis and more, texture of materials, in: J.A. Spunar (Ed.), Proceeding of the ICOTOM14, National Research Council of Canada, Ottawa, 1999, pp. 1599–1604.

[20] S. Matthies, G. Vinel, K. Helming, in: S. Matthies, G. Vinel, K. Helming (Eds.), Standard Distributions in Texture Analysis, vol. 1, Akademie-Verlag, Berlin, 1987, pp. 1–449.

[21] L. Lutterotti, D. Chateigner, S. Ferrari, J. Ricote, Thin Solid Films 450 (2004) 34–41.

[22] D. Chateigner, J. Appl. Crystallogr. 38 (2005) 603–611.

[23] E. Guilmeau, D. Chateigner, J. Noudem, R. Funahashi, S. Horii, B. Ouladdiaf, J. Appl. Crystallogr. 38 (2005) 199–210.

[24] W.C. Oliver, G.M. Pharr, J. Mater. Res. 7 (1992) 1564–1583.

[25] J. Woirgard, J.C. Daegenton, J. Mater. Res. 12 (1997) 2455–2458.

[26] J.G. Noudem, J. Eur. Ceram Soc. 29 (2009) 2659–2663.

[27] Y. Liu, Y. Lin, Z. Shi, C.W. Nan, J. Am. Ceram. Soc. 88 (2005) 1337–1340.